Macromolecules

ARTICLE

pubs.acs.org/Macromolecules

# Surfactant-Free Synthesized Magnetic Polypropylene Nanocomposites: Rheological, Electrical, Magnetic, and Thermal Properties

Jiahua Zhu,[†] Suying Wei,[‡] Yutong Li,[§] Luyi Sun,[⊥] Neel Haldolaarachchige,[∥] David P. Young,[∥] Cara Southworth,[⊥] Airat Khasanov,[#] Zhiping Luo,[○] and Zhanhu Guo[†,*]

[†]Integrated Composites Laboratory (ICL), Dan F. Smith Department of Chemical Engineering, Lamar University, Beaumont, Texas 77710, United States

[‡]Department of Chemistry and Biochemistry, Lamar University, Beaumont, Texas 77710, United States

[§]Magnetic Head Operation, Western Digital Corporation, Fremont, California 94539, United States

[⊥]Department of Chemistry and Biochemistry, Texas State University—San Marcos, San Marcos, Texas 78666, United States

[∥]Department of Physics and Astronomy, Louisiana State University, Baton Rouge, Louisiana 70803, United States

[#]University of North Carolina at Asheville, Asheville, North Carolina 28804-8511, United States

[○]Microscopy and Imaging Center, Texas A&M University, College Station, Texas 77843, United States

**ABSTRACT:**

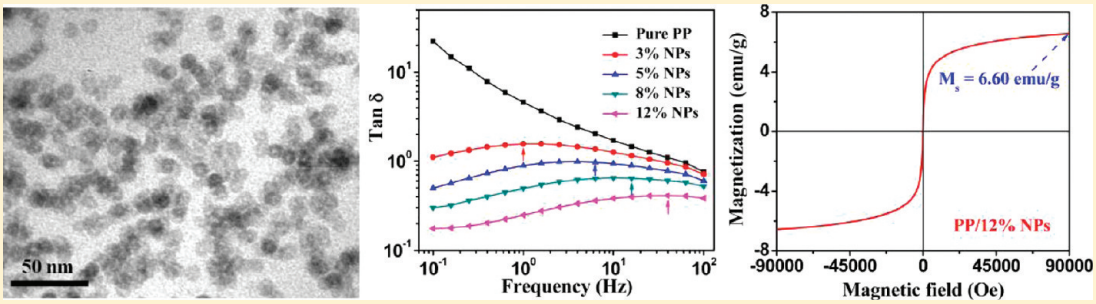


A facile surfactant-free process is introduced to prepare multifunctional polypropylene (PP) nanocomposites filled with highly dispersed Fe@$Fe_2O_3$ core@shell nanoparticles (NPs). Transmission electron microscopy (TEM) observations confirm the formation of uniform NPs in the PP matrix and the particle size increases with increasing the particle loading. The melt rheology measurements show an obvious change in the frequency dependent storage modulus ($G'$), loss modulus ($G''$) and complex viscosity ($\eta^*$) particularly at low frequencies. These changes are often related to the filler "percolation threshold", which has also been verified in the sharp change of electrical resistance and dielectric permittivity of these nanocomposites in higher particle loadings. The continuous decrease in the resistivity with increasing filler loading from 5 wt % to 20 wt % demonstrates the structural transition of the nanocomposites. The monotonic increase in the dielectric permittivity with increasing particle loadings combined with the direct evidence from the TEM observations indicate that the NPs are well separated and uniformly dispersed in the polymer matrix. Thermal gravimetric analysis (TGA) results reveal a surprisingly high enhancement of the thermal stability by ~120 °C in air due to the oxygen trapping effect of the NPs and the polymer−particle interfacial interaction. The differential scanning calorimetry (DSC) results show that the crystalline temperature ($T_c$) of the nanocomposites is reduced by 16−18 °C as compared to that of PP, while the melting temperature ($T_m$) almost maintains the same. The nanocomposites is found to be soft ferromagnetic at room temperature.

## 1. INTRODUCTION

Over the past few decades, magnetic materials with various shapes and sizes have demonstrated wide potential applications, for examples, in data storage,[1,2] magnetic sensors,[3−5] biomedical[6,7] (i.e., drug delivery) and pharmaceutical areas[8,9] and even the environmental remediation.[10] Polymer nanocomposites (PNCs) have been well developed in the last 2 decades due to the combined advantages of polymers, such as lightweight, easy processability and flexibility, and excellent physiochemical characteristics of the inorganic nanomaterials such as high mechanical strength and excellent electrical, magnetic and optical properties. Therefore, magnetic PNCs have attracted wide interest for their diverse

**Received:** November 24, 2010
**Revised:** March 14, 2011
**Published:** May 10, 2011

potential applications such as energy storage devices,[11] electrochromic devices,[12] electronics,[13,14] microwave absorbers,[15,16] and sensors.[17]

The major challenge lying ahead to obtain high performance PNCs comes from the serious agglomeration of the nanomaterials owing to their high surface energy and large specific surface area. Thus, a lot of efforts have been made to tailor their surface property through physical and chemical approaches[18−21] to improve the interfacial compatibility between the inorganic fillers and the polymer matrix. To overcome the challenges in dispersing the magnetic nanoparticles (NPs) limited by the magnetically induced agglomeration, techniques including encapsulating the magnetic core with surfactant,[22] polymer,[23] silica,[24] and carbon[10] have been reported. However, these well-dispersed NPs can only be limitedly applied in specific polymers with versatile surface functionalities. Right now, most of the current research work on fabricating PNCs starts from the as-prepared NPs and polymers (or monomer) with a direct blending[14] or surface initiated polymerization method.[25] A general method is of great interest to simplify the procedures while maintaining the well-dispersed magnetic NPs.

The critical concentration of the fillers within the polymer matrix, where the performance of the PNCs experiences a sharp change, is often called "percolation threshold". Almost all the physical properties, including viscoelastic, thermal, mechanical and electrical properties are related to the percolation phenomenon. Thus, various methods are developed to determine the percolation value. Most of the current research efforts concentrate on the carbon based nanomaterials such as carbon nanotubes (CNTs),[26] carbon nanofibers,[13,27] carbon NPs,[28] and graphene[29] to enhance the thermal, electrical and mechanical properties of the polymers. Nanoclays[30,31] are often used to improve the fire retardant performance. Pötschke et al.[32] studied the rheological and dielectric percolation of the multiwalled CNTs/polycarbonate PNCs and found that the rheological percolation (0.5−5 wt %) is strongly dependent on the temperature and the electrical percolation is at about 1 wt %. Sandler et al.[33] reported a ultra low electrical percolation in the CNTs/epoxy PNCs at a loading of 0.0025 wt %. It is well-known that the percolation threshold is also dependent on the filler morphology, spherical particles are relatively difficult to reach percolation as compared to those with larger aspect ratio (like fibers and tubes). Therefore, a relatively higher loading of around 16 vol % from geometrical model[34,35] is required to reach percolation. Recently, Zhu et al. reported a low electrical percolation at 1.5 vol % with spherical Fe(core)−FeO(shell) structured NPs in epoxy resin using a surface wetting method.[14]

In this work, we report a facile in situ surfactant free method to synthesize magnetic polyolefin polypropylene (PP) nanocomposites. The magnetic NPs are produced using $Fe(CO)_5$ as a precursor during the refluxing process in the $Fe(CO)_5$/PP/xylene solution. The as-synthesized NPs are physically wrapped by PP. Rheological, electrical, and dielectric percolation behaviors are studied. The percolation mechanisms of the particle−PP interaction are discussed in this work. The magnetic and thermal properties of these PNCs are also investigated.

## 2. EXPERIMENTAL SECTION

**2.1. Materials.** The isotactic PP used in this study was supplied by Total Petrochemicals Inc. USA, (0.9 g/cm$^3$ in density, $M_n \approx 40500$, $M_w \approx 155000$, melt index ≈ 35 g/min). Iron(0) pentacarbonyl (iron carbonyl, $Fe(CO)_5$, 99%) is commercially obtained from Sigma-Aldrich. The solvent xylene (laboratory grade, $\rho$ = 0.87 g/cm$^3$) with a boiling temperature ranging from 137 to 145 °C was purchased from Fisher Scientific. All the chemicals were used as received without any treatment.

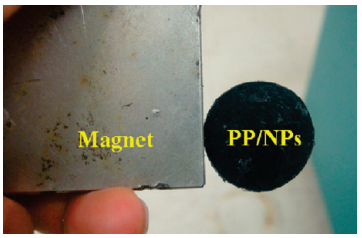


**Figure 1.** Prepared magnetic nanocomposite sample attached to a magnet.

**2.2. Fabrication of Polymer Nanocomposites.** PP was initially dissolved in xylene with a weight ratio of 1:10 (20 g: 207 mL) and refluxed at the boiling point (∼140 °C) of xylene for around 2 h until PP was completely dissolved. Then different weight (2.17, 3.67, 6.08, 9.54, and 17.48 g) of liquid $Fe(CO)_5$ was injected into the dissolved PP solution to obtain the final PNCs containing 3, 5, 8, 12, and 20 wt % of the NPs (based on pure iron element). The mixture solution turned from transparent to yellow immediately after the addition of $Fe(CO)_5$ and then gradually changed to black during the additional 3-h refluxing process under the nitrogen protecting conditions, indicating the formation of the NPs. The PNC solution was then cooled down to around 90 °C and then poured onto a large glass plate to allow solvent evaporation overnight. The powder-like products were collected and kept in a vacuum oven at room temperature overnight. Pure PP powders are also prepared following the above procedures without adding $Fe(CO)_5$ and are termed as p-PP to differentiate from the as-received PP (o-PP).

Upon heating, $Fe(CO)_5$ was decomposed to $Fe_2(CO)_9$ and $Fe_3(CO)_{12}$ with a rapid formation of CO, reaching an equilibrium mixture of all the three carbonyls. The $Fe_3(CO)_{12}$ was then decomposed and finally formed the metallic NPs.[36,37] Oxidization took place on the surface and then a core−shell structure was formed after exposure to air.

The desired samples are prepared from PP both the as-received original PP (o-PP) and processed PP (p-PP) and its PNC powders using hot press (Carver 3853-0, USA). Briefly, the dried powders were compressed under a pressure of 10 MPa at 180 °C in a mold at a heating rate of 20 °C/min. The compressed composites were held at 180 °C for 20 min and then cooled down to room temperature in the mold while maintaining the applied pressure. Finally, a disk-shaped nanocomposite sample was prepared with a diameter of 25 mm and thickness of 2−3 mm. Figure 1 shows the prepared PNCs magnetically attracted by a magnet.

**2.3. Characterization.** Fourier transform infrared spectroscopy (FT-IR, Bruker Inc. Tensor 27) with hyperion 1000 ATR microscopy accessory was used to characterize PP and its PNCs over the range of 2500 to 400 cm$^{-1}$ at a resolution of 4 cm$^{-1}$. The X-ray diffraction (XRD) analysis with Cu radiation source was carried out with a STA Jupiter 449C (Netzsch) on disk samples with a diameter of 25 mm.

The particle distribution in the PP matrix was examined by a transmission electron microscope (TEM). The samples were stained in $RuO_4$ vapor to harden the surface and then microtomed into a film with a thickness of ∼100 nm, which were observed in a JEOL 2010 TEM at a working voltage of 200 kV. Images were recorded with a Gatan Orius SC 1000 CCD camera. In order to obtain more accurate particle size, magnifications were calibrated using commercial cross-line grating replica and SiC lattice images.[38]

The rheological behavior of the PNCs was studied using TA Instruments AR 2000ex Rheometer. An environmental test chamber (ETC) steel parallel-plate geometry (25 mm in diameter) was used to perform

the measurement at 200 °C, with dynamic oscillation frequency sweeping from 100 to 0.1 Hz in the linear viscoelastic (LVE) range (strain 1%) under a nitrogen atmosphere to prevent the oxidation of PP.

The thermal degradation/stability of the PNCs was studied with a thermo-gravimetric analysis (TGA, TA Instruments TGA Q-500) from 25 to 600 °C in air and nitrogen atmosphere, respectively, with a flow rate of 60 mL/min and a heating rate of 10 °C/min. Differential scanning calorimeter (DSC, TA Instruments Q2000) measurements were carried out from 0 to 250 °C under a nitrogen flow rate of approximately 100 mL/min at a heating rate of 10 °C/min.

The volume resistivity was determined by measuring the DC resistance on a disk-shaped sample (diameter, ~50 mm; thickness, 0.5−1.0 mm). An Agilent 4339B high resistance meter equipped with a resistivity cell (Agilent, 16008B) was used to measure the volume resistivity of each sample after inputting the thickness. This equipment allows the resistivity measurement up to $10^{16}\Omega$. The source voltage was set at 0.1 V for all the samples. The reported values represent the mean value of eight measurements with a deviation less than 10%.

The dielectric properties were measured by a LCR meter (Agilent, E4980A) equipped with a dielectric test fixture (Agilent, 16451B) at the frequency of 20 HZ-2 MHz. The PP and PNCs were hot pressed in the form of disk pellets with a diameter of 60 mm and an average thickness of about 0.7 mm.

The magnetic property measurements of the PNCs with various particle loadings were carried out in a 9 T physical properties measurement system (PPMS) by Quantum Design at room temperature.

## 3. RESULTS AND DISCUSSION

**3.1. FT-IR Analysis.** Figure 2 shows the FT-IR spectra of pure PP and its PNCs. The absorption peaks at 1455 and 1375 $cm^{-1}$ are attributed to the C−H bending vibration of the polymer matrix, and the multi peaks near 3000 $cm^{-1}$ are assigned to the C−H stretching vibration.[39] These characteristic peaks are well maintained in all the PNC samples, indicating that the polymer structure is not changed in the PNCs fabricated by this in situ thermo-decomposition method. A new broad peak at around 550 $cm^{-1}$ corresponding to the vibration Fe−O modes[40,41] in $Fe_2O_3$ is observed. The peak strength becomes more intense with increasing particle loading with respect to the other peaks in each FT-IR curve, which is due to the presence of more NPs in the polymer matrix with an increased particle loading.

**3.2. Microstructure of PNCs and Electron Diffraction of NPs.** Figure 3 shows the TEM micrographs of the PNCs containing 5, 8, and 20 wt % NPs at two different magnifications. The NPs are observed to be uniformly distributed in the polymer matrix and the particle size is well controlled, demonstrating that this in situ method is effective to synthesize PNCs with highly uniform NPs. The measured particle size (from Figure 3, parts b, d, and f) increases gradually with increasing particle loading. The average particle diameter is 8.2 ± 1.2, 11.0 ± 0.9, and 15.9 ± 2.2 nm for PNCs reinforced with a particle loading of 5, 8, and 20 wt %, respectively. In most cases, the particle size is governed by the rates of nucleation and growth.[42] Since the same precursor and synthesis procedures are used during the preparation of different PNCs in this work, the nucleation rate should be the same. The larger particle size obtained at higher loading is due to the growth of more concentrated nucleates in the unit volume.

To obtain the phase structure of the formed NPs, the NPs are characterized by high resolution TEM (HRTEM), Figure 3g. The fringe spacing is about 2.60 and 2.20 Å, corresponding to the (104) and (113) crystal planes of $Fe_2O_3$. The corresponding selected area electron diffraction (SAED) pattern is presented in Figure 3h. The rings with plane distances of 2.60, 2.20, 1.70, and 1.39 Å are observed, which fit well with the (104), (113), (116), and (214) diffraction planes for the trigonal phase of $Fe_2O_3$.[43,44]

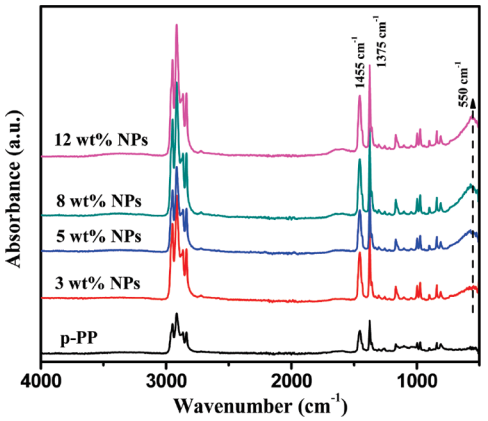


**Figure 2.** FT-IR spectra of p-PP and its PNCs with different particle loadings.

The percolation (or called threshold), which is essentially important for the prediction and interpretation of the switching physical phenomena, can be observed from the particle−particle interaction within the polymer matrix. Once a network structure of the filler is formed in the composites, the electrical,[13,45] rheological[27] and mechanical properties[46] will experience a sharp change. The PNCs with the particle loading increasing from 5 to 20 wt % illustrate the structural transition of the NPs within the polymer matrix. For 5 wt % loading, the NPs are loosely embedded in the matrix, though continuous network structure can not be observed, the string-like particle chain begins to form, Figure 3a. When the loading increases to 8 wt %, the NPs are distributed more densely and the particle−particle distance is significantly reduced. The network structure of the NPs is completely formed as the loading reaches 20 wt %, meanwhile some agglomerates are observed due to the high particle packaging density in the unit volume.

**3.3. X-ray Diffraction and Mössbauer Analysis.** Despite the simplicity of its chemical component, PP shows a remarkable complexity of crystal structures (phases), which include α, $\beta$, and $\gamma$ phases. Each of the α, $\beta$, and $\gamma$ crystalline form has its own distinctive peaks in the XRD patterns. Figure 4 shows the XRD profiles of PP and its PNCs. It is obvious that the peak intensity decreases gradually with increasing particle loading, which is attributed to the decreased crystalline size of PP after introducing the NPs (the crystallinity is almost maintained from the DSC analysis, Table 1).

In a typical XRD pattern of the α phase PP, the intensity of the first peak (110) is always stronger than that of the second peak (040).[47] However, it is not true for the samples containing $\gamma$ phase. All the samples are characterized by a stronger second peak than that of the first one, which is not surprising considering the same location of the strong peak in $\gamma$ phase. Because of the high diffraction similarity between α and $\gamma$ phases in the region of 13−17°, the $\gamma$ phase is usually determined from the peak at $2\theta$ = 20.07° (117), and α phase is identified from the peak $2\theta$ = 18.50° (120).[48] The other peaks at $2\theta$ = 14.06, 16.90, 21.20, and 21.86 ° correspond to the 110, 040, 131, and 041 crystalline planes of α-PP, respectively. It is interesting to observe that the peak intensity at $2\theta$ = 20.07° decreases with the addition of the NPs. However, the amount of $\gamma$-PP shows a surprisingly filler

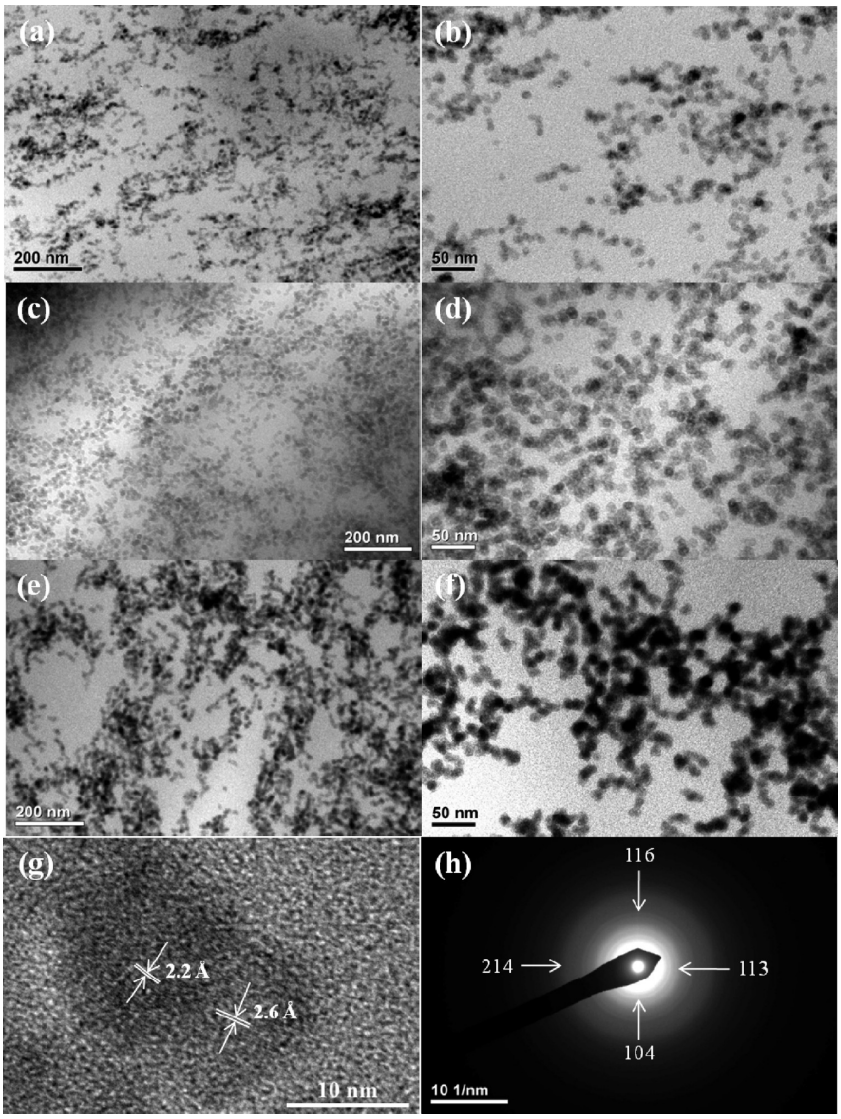


**Figure 3.** TEM images of the PNCs with a particle loading of (a and b) 5, (c and d) 8 and (e and f) 20 wt %; (g) HRTEM and (h) SAED pattern of the NPs.

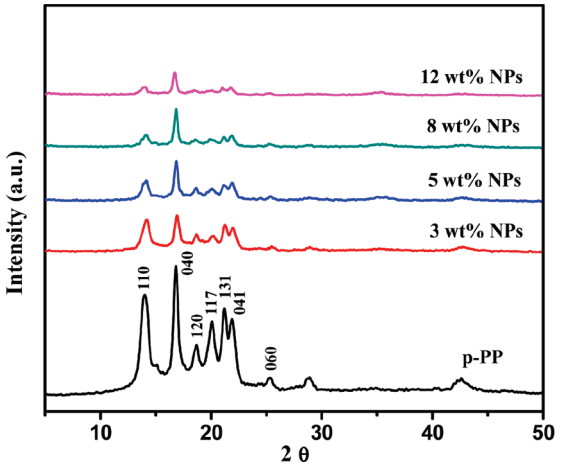


**Figure 4.** X-ray diffraction patterns for p-PP and its PNCs.

loading independent behavior and a comparable peak intensity at $2\theta = 20.07°$ is observed as compared to that of the peak at $2\theta = 18.50°$. In a previous study,[49] the ratio of $\gamma$ to $\alpha$ is simply calculated from the relative intensity of the unique peaks of $\gamma$ phase at $2\theta = 20.07$ and $\alpha$ phase at $2\theta = 18.50°$. The relatively low intensity of the peak at 20.07° as compared to that of the peak at 18.50° after the incorporation of the NPs suggests a reduced amount of $\gamma$ phase during the crystallization process. Earlier studies show that more PP is observed to be crystallized in the $\gamma$ phase at a lower cooling rate.[50] In this case, the conductive fillers within the polymer matrix create a pathway for heat transfer and the cooling rate is much faster for the PNCs as compared to that of pure PP, which is observed in the CNTs suspended in

**Table 1. DSC Characteristics of p-PP and Its PNCs**

| material | $T_m$ (°C) | $\Delta H_m$ (J/g) | $T_c$ (°C) | $\Delta H_c$ (J/g) | $F_c$ (%) |
|---|---|---|---|---|---|
| p-PP | 149.2 | 90.4 | 119.8 | 86.6 | 43.3 |
| 3 wt % NPs | 148.6 | 80.8 | 103.4 | 83.0 | 39.9 |
| 5 wt % NPs | 149.1 | 86.7 | 101.6 | 89.1 | 43.6 |
| 8 wt % NPs | 148.1 | 63.8 | 101.3 | 66.4 | 42.9 |
| 12 wt % NPs | 149.3 | 67.5 | 101.3 | 66.8 | 36.7 |


dx.doi.org/10.1021/ma102684f |*Macromolecules* 2011, 44, 4382–4391

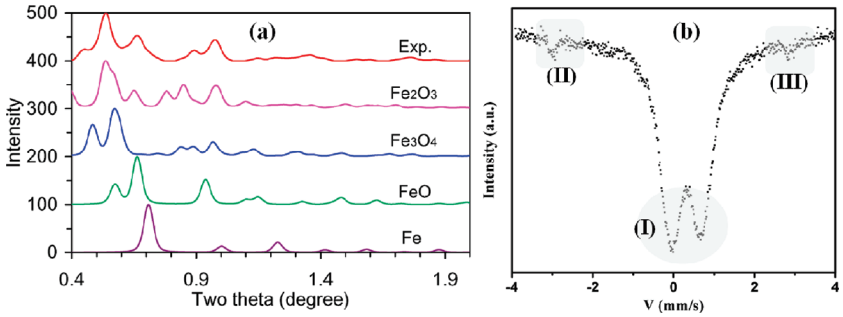


**Figure 5.** (a) Experimental and simulation results of the NPs from TEM-SAED patterns, and (b) Mössbauer spectra of the PNCs with particle loading of 20 wt %.

surfactant micelles in water.[51] Therefore, a decreased amount of PP in $\gamma$ phase is observed.

However, no additional peak regarding the NPs is detected in the PNCs as compared with those of pure PP, which is due to the limitation of the XRD whose signals only come from the sample surface. The crystalline structure of the NPs was further identified from the comparison between the experimental and simulated TEM-SAED patterns. Mössbauer analysis was also used to justify the valence of iron in the NPs.

The particle composition is examined by the consistence between the experimental and simulation results based on the SAED data.[52] To be specific, the intensity profile of the SAED pattern is measured using ELD program[53] and the background of the intensity profile is subtracted using Reflex module in MS Modeling program.[52] Then the simulated SAED powder patterns are calculated using the standard structures of $Fe_2O_3$, $Fe_3O_4$, FeO and Fe. In comparison with the peak position and intensities, $Fe_2O_3$ fits the experimental observation the best, Figure 5a. However, there is still difference between the experimental curve and the standard simulated $Fe_2O_3$ pattern. To further confirm the particle composition, room temperature Mössbauer spectrum analysis is conducted on the PNCs with a particle loading of 20 wt %, Figure 5b. The paramagnetic doublet observed in the center of the Mössbauer spectra, Figure 5b(I), confirms the existence of $Fe^{3+}$, which corresponds to the superparamagnetic behavior of $Fe_2O_3$.[54] The fitting results show a main component at isomer shift (IS) = 0.35 mm/s and quadrupole splitting (QS) = 0.80 mm/s, which is $Fe^{3+}$ in a paramagnetic state in the distorted oxygen octahedral site. Figure 5b(II,III) depicts the secondary component with IS = 0 and correspondent $H$ = 335 kOe, which represents a spectral contribution of 5% α-Fe metallic magnetically ordered state. The aforementioned analysis justifies that the formed NPs have a chemical structure of Fe core and $Fe_2O_3$ shell.

**3.4. Melt Rheology.** The rheological behaviors of the composite melts are essentially important for industrial nanocomposite processing. Also, the formation of a percolated system can be detected by characterizing the complex viscosity ($\eta^*$), storage modulus ($G'$), and loss modulus ($G''$) as a function of frequency.[13,27,32,55] Figure 6 shows the variation of $\eta^*$ with frequency for pure PP and its PNCs measured at 200 °C. $\eta^*$ increases with increasing the particle loading, especially at low frequency such as 0.1 Hz. Pure PP is observed to have frequency independent fluid properties, i.e., Newtonian-type flow only within the range of 0.1−0.4 Hz and shear thinning (viscosity decreases with an increase of shear rate/frequency) dominates the melt thereafter until 100 Hz.[56,57] The PNCs with a particle

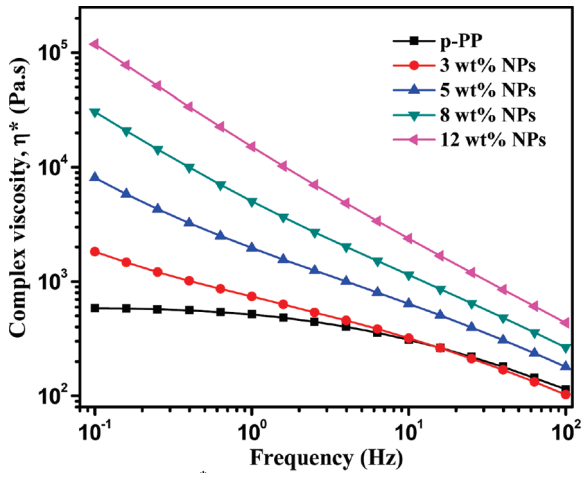


**Figure 6.** Complex viscosity ($\eta^*$) as a function of frequency for PP and its PNCs.

loading of 3 wt % are much more viscous than that of pure PP at low frequencies and exhibit strong shear thinning behavior. The similar value of $\eta^*$ at high frequency (10−100 Hz) indicates a polymer melt rather than filler dominated fluid dynamics. However, as the particle loading increases to 5, 8, and 12 wt %, the viscosity curve becomes linear within the whole frequency range. This phenomenon indicates a filler dominated fluid in the PNCs with a relatively high particle loading. The transition in $\eta^*$ indicates that the PNCs have reached a rheological percolation, at which the NPs form a network structure and greatly impede the motion of the polymer chains. The increase of $\eta^*$ with an increase of particle loadings is primarily due to the significant increase in $G'$ and $G''$ ($\eta^* = \eta' - i\eta''$, where $\eta' = G''/\omega$, $\eta'' = G'/\omega$. $\omega$ is angular frequency, rad/s).[58]

At 200 °C, the PP chains are fully relaxed and exhibit a typical homopolymer-like terminal behavior, which disappears with the addition of the NPs. $G'$ increases monotonically with increasing the particle loading at all frequencies, Figure 7a. Larger enhancement of $G'$ with orders of magnitude is observed at lower frequencies for the PNCs, which indicates that the large-scale polymer chain relaxations in the PNCs are significantly restrained by the presence of the NPs. The $G'$ versus frequency curve for the PNCs with relatively higher particle loadings (≥5 wt %) approaches a plateau at low frequencies. This "plateau" with a nonterminal low-frequency behavior[59] suggests either an interconnected structure of the fillers or a strong particle−polymer interaction.[32] Similar low frequency response was also

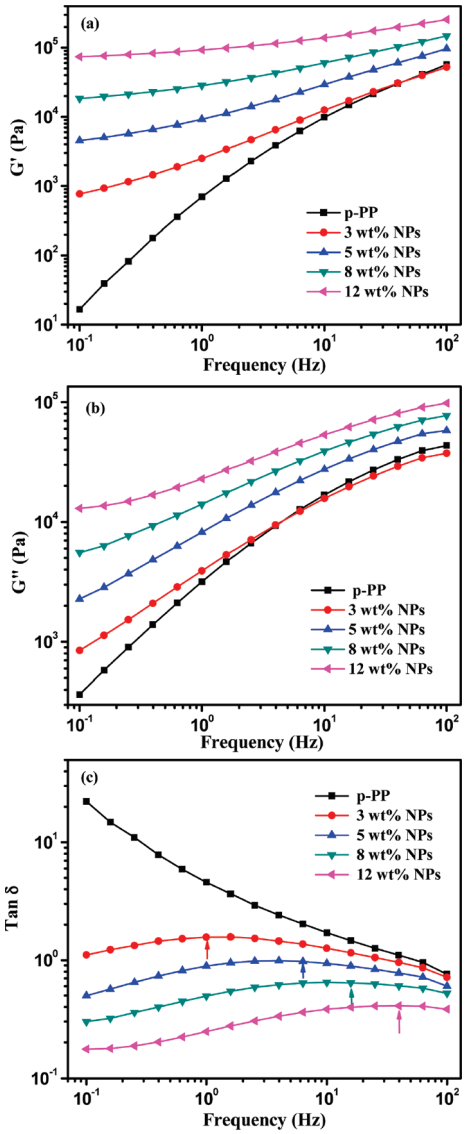


**Figure 7.** (a) Storage modulus ($G'$), (b) loss modulus ($G''$), and (c) tan $\delta$ as a function of frequency for PP and its PNCs (the peak position is marked with arrow).

observed in the conventional composites.[60,61] At high frequencies, the effect of the particle loading on the rheological behavior is relatively weak. This phenomenon indicates that the NPs are not effective to affect the short-range dynamics of the PP chains.[59] Similar curve of the $G''$ with increasing frequency is observed, Figure 7(b). The plateau is observed in the PNCs with higher particle loading ($\geq$8 wt %).

The tan $\delta$ is the ratio of $G''$ to $G'$, which is used to characterize the damping property of the PNCs. It is obvious that tan $\delta$ decreases and the corresponding curves become flatter with increasing particle loading, Figure 7c. The mechanical loss, which is arising from the discordance between strain and stress in the polymer exposed to an external force,[62] is strongly related to the applied frequency. The tan $\delta$ of pure PP decreases monotonously, while a peak is observed in all the PNC samples. The higher tan $\delta$ of pure PP than that of the PNCs is due to the fully relaxation of the PP chains, which makes the interpolymer-chain motion more difficult and more interchain friction heat is

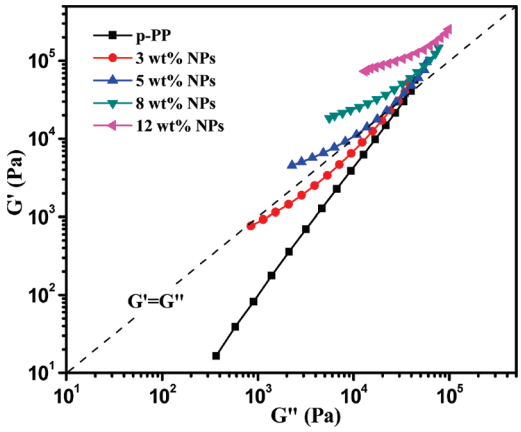


**Figure 8.** Storage modulus ($G'$) as a function of loss modulus ($G''$) for PP and its PNCs.

generated during the oscillation. After incorporating the NPs, the polymer chain relaxation and relative motion have been greatly restrained by the presence of the NPs and the PNCs are "stiffer". Therefore, less internal chain−chain friction heat is produced upon applying the same oscillation frequency. In addition, the higher the particle loading, the lower tan $\delta$ is observed. This observation suggests a strong interaction between the NPs and the polymer matrix, both energy dissipation and relaxation of the PP chains are increasingly hindered as the particle loading increases. For the PNCs, a broad peak appears on each tan $\delta$ curve and the peak position shifts to higher frequency with increasing nanoparticle loading due to the greater restrictions. At low frequency, the polymer chain motion keeps in step with the oscillation and the internal friction among the polymer chains would be neglected. Once the frequency goes to extremely high, the movement of the polymer chains is not able to catch up the variation of the frequency. Therefore, the PNCs behave like glass state and generate small amount of energy loss. Large amount of energy loss appears between these two extreme conditions when the polymer shows viscoelastic properties.[63] Similar phenomena have been observed in the PP/carbon nanofiber nanocomposites.[64]

$G'$ versus $G''$ for the PP and its PNCs is plotted in Figure 8. Generally, $G'$ increases with the increase of $G''$. The structural difference of each composite can be monitored from the slope change of the curves. The gradually decreased slope evidence the structural change as the particle loading increases, which is also observed in the MWCNT reinforced polycarbonate[32] and polyethylene[61] PNCs.

**3.5. Electrical Conductivity.** Figure 9 shows the electrical conductivity ($\sigma$) of the PNCs with different nanoparticle loadings. Three distinct stages could be identified on the conductivity curve. The addition of 3 wt % NPs shows a negligible reduction in the resistivity with the same order of magnitude ($\sim 10^{13}$ $\Omega \cdot$cm), indicating an insulator behavior. As the nanoparticle loading increases to 5 wt %, the resistivity begins to decrease owing to the tunneling effect between the neighboring NPs. With further increasing particle loading, the resistivity of the PNCs decreases significantly and is reduced by 6 orders of magnitude ($\sim 10^{7}$ $\Omega \cdot$cm) when the particle loading reaches 12 wt % ($\sim$2.3 vol %). After that, further addition of the particle loading does not contribute to the reduction of the resistivity. Comparing with the prominent geometrical models created by Kirkpatrick[34] and


dx.doi.org/10.1021/ma102684f |*Macromolecules* 2011, 44, 4382–4391

Zallen,[35] the required minimum touching spherical particle loading is 16 vol %, which is in approximately agreement with most experimental observations that the critical volume fraction is between 5 and 20 vol % for PNCs filled with powdery materials. The lower observed percolation threshold 5−12 wt % (0.96−2.3 vol %) in this work is primarily attributed to the small particle size and good dispersion of the NPs from this in situ method, as evidenced by the TEM observations, Figure 3.

The inset of Figure 9 depicts the $G'$ and $G''$ against filler loading at the low oscillation frequency of 0.1 Hz, in which the crossing point is used to determine the rheological percolation of the PNCs.[27] The observed rheological percolation is about 3.4 wt % (0.65 vol %), which is much lower than the electrical percolation of 5−12 wt % (0.96−2.3 vol %). Figure 10 shows the schematic model of the gradually formed particle percolation. The NPs are physically wrapped with polymer chains due to their large specific surface area and their strong affinity with the surrounding media, which form a particle complex (the thickness of the polymer wrapping layer plus the radius of the NPs). The formed nanoparticle complex is actually larger than the radius of the bare NPs. This "real radius" is particularly effective in the rheological properties. Once the distance between the NPs gets close to double of the "real radius", the wrapped NPs form an interconnected network, which is called "rheological percolation". However, the resistivity analysis indicates that this distance is not close enough to form a network structure for the electrons to pass through the neighboring NPs as a "tunneling effect" (the resistivity does not change with 3 wt % NPs). Therefore, a higher particle loading is needed to reach the electrical percolation. While increasing the filler loading from 5 to 8 wt %, the reduced interparticle distance leads to the "tunneling effect" and meanwhile the network structure begins to form, thus a gradually decreased resistivity is observed. The resistivity reaches a saturation value at the loading of 12 wt % and it does not change as the filler loading further increases to 20 wt %. This indicates that a network of NPs has been formed completely at the loading of 12 wt % and the significantly reduced resistivity is due to the electron pathway created by the direct contact of the NPs.

**3.6. Dielectric Properties.** Parts a and b of Figure 11 show the room temperature real permittivity ($\varepsilon'$) and imaginary permittivity ($\varepsilon''$) as a function of frequency for pure PP and its PNCs

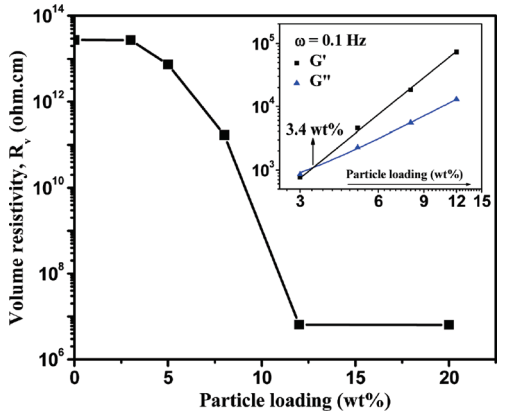


**Figure 9.** Change of volume resistivity as a function of nanoparticle loading.

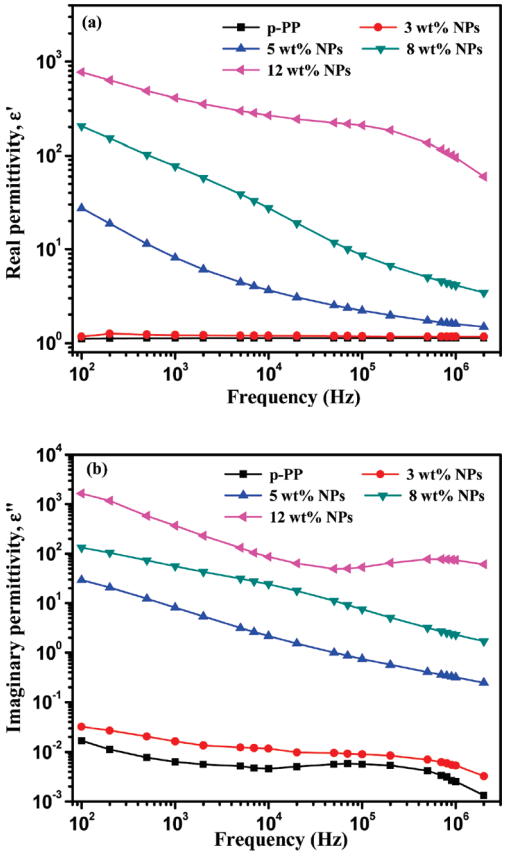


**Figure 11.** (a) Real permittivity ($\varepsilon'$), and (b) imaginary permittivity ($\varepsilon''$) as a function of frequency for PP and its PNCs.

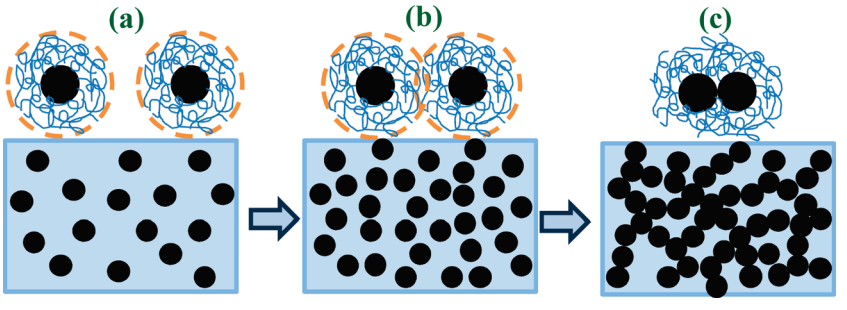


**Figure 10.** Schematic illustration of the gradually formed nanoparticle percolation. The polymer chains wrapped on the NPs and formed a "real radius" (the radius of the orange circle). Key: (a) separated NPs from both rheological and electrical percolation points, (b) rheologically interconnected NPs, and (c) electrically interconnected NPs.

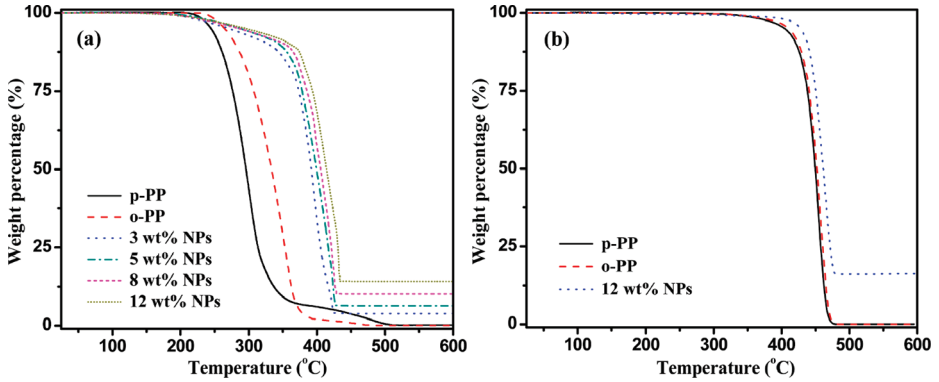


**Figure 12.** Thermogravimetric curves of PP and its PNCs (a) in air and (b) in nitrogen.

with different nanoparticle loadings. Pure PP and PNCs with a nanoparticle loading of 3 wt % are observed to exhibit constant $\varepsilon'$ value, Figure 11a. However, the PNCs with particle loadings larger than 3 wt % show a dielectric relaxation behavior ($\varepsilon'$ decreases with increasing frequency). This result is in good agreement with the variation of electrical resistance of the PNCs, where a transition starts from the concentration of 5 wt % (often called "percolation"). It is worth noting that both $\varepsilon'$ and $\varepsilon''$ of the PNCs are enhanced significantly by orders of magnitude near the percolation, Figure 11, parts a and b, respectively. The obtained $\varepsilon'$ value is 770 for the PNCs with 12 wt % filler loading, which is about 700 times larger than that of pure PP. The significantly enhanced real dielectric permittivity indicates that the thin insulating PP layer physically wrapped on the nanoparticle surface is still dielectrically strong to hold the charge carriers in the NPs at low frequency. The dielectric permittivity of the PNCs with filler content higher than 3 wt % decreases toward high frequency, suggesting that the insulating layer is not stable and easily affected by the external frequency disturbance. Similar observations are also observed in the MWCNT/poly-(vinyldenefluoide) PNCs.[65]

**3.7. Thermal Properties.** Figure 12a shows the TGA curves of PP and its PNCs with different particle loadings tested in the air flow condition. The p-PP shows an onset decomposition temperature ($T_d$) of 251.8 °C, while the o-PP shows a higher $T_d$ at 265.7 °C, Figure 12a. The decreased thermal stability of the p-PP after processing indicates a reduced interaction between polymer chains and an easy degradation of PP with the air after processed with solvent. A much higher $T_d$ of 370.0, 373.5, 382.9, and 384.0 °C is observed in the PNCs with a nanoparticle loading of 3, 5, 8, and 12 wt %, respectively. In order to disclose the role of the NPs especially with a metal core in the decomposition of the PP, the samples were also tested in a nitrogen flow condition. Only slight thermal stability improvement is observed, Figure 12b, which is due to the strong interfacial particle−polymer interaction and is also observed in other polymer nanocomposite systems.[66−69] In addition, o-PP and p-PP are observed to have similar thermal stability, Figure 12b, indicating that air promotes the degradation of PP as well after processed with solvent, Figure 12a. The tremendous thermal stability improvement of around 120 °C as compared to p-PP is due to the presence of the NPs, especially with a metal core, as evidenced by Mössbauer spectra, Figure 5(b). Operated in the air condition, iron acts as oxygen trap and thus reduces the oxidation effect of oxygen on the PP molecular chains to give a higher decomposition temperature. The actual residue is 3.6, 6.1, 9.9, and 13.9% for the PNCs reinforced with 3, 5, 8, and 12 wt % NPs, respectively. The theoretically calculated residue based on the NPs is 3.8, 7.0, 11.0, and 16.6%. These slightly higher values than the corresponding actual residues are primarily due to the evaporation of small amount of $Fe(CO)_5$ during the reflux process.

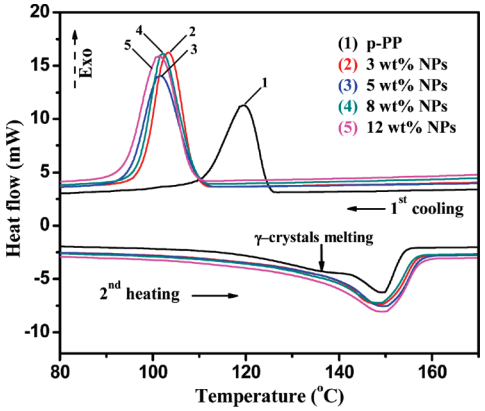


**Figure 13.** DSC cooling (first cycle) and heating (second cycle) curves for pure PP and its PNCs.

To remove the effect of heat history on the obtained heat data, all the samples are first heated to 250 °C with a heating rate of 10 °C/min under nitrogen, allow the samples to maintain at 250 °C for 2 min and then cool down to room temperature with a cooling rate of 10 °C/min. Immediately after that, the samples are heated again to 250 °C following the same procedures as used for the first heating process. The DSC curves are recorded using the data collected on the first cooling and second heating processes, Figure 13. The melting temperature ($T_m$) of PP is not affected by the addition of the NPs. However, the crystalline temperature ($T_c$) of PP is decreases by 16−18 °C, where PP is crystallized at 119.8 °C and the PNCs are crystallized at 101−103 °C. The lowered $T_c$ is attributed to the strong particle−polymer interaction, which greatly restricts the segmental motion of the polymer chains and inhibits the content of the crystalline structures in the polymer chains. The lowered peak intensity in XRD curves with increasing particle loading together with the crystalline fraction calculated from DSC further confirm this observation. The broad peak from 125 to 145 °C in pure PP curve is due to the melting of the $\gamma$-crystals, while this peak is not observed in the PNCs. This observation is quite consistent with the XRD results that the decreased peak intensity at $2\theta = 20.07°$ (117) corresponds to a lower content of $\gamma$-phase PP in the PNCs.


dx.doi.org/10.1021/ma102684f |*Macromolecules* 2011, 44, 4382–4391

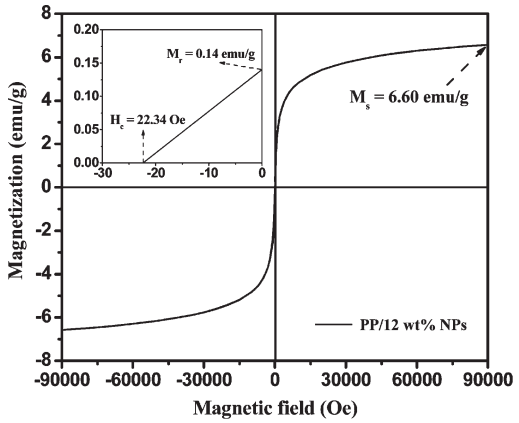


**Figure 14.** Room temperature hysteresis loop of the PNCs with a 12 wt % particle loading.

Table 1 lists the DSC characteristics of PP and its PNCs. The crystalline fraction ($F_c$) of the polymer within the PNCs is calculated from eq 1

$$F_c = \frac{\Delta H}{209 f_P} \quad (1)$$

where $\Delta H$ is the enthalpy of fusion (J/g), 209 J/g is the fusion enthalpy for a theoretically 100% crystalline PP[70] and $f_p$ is the weight fraction of the polymer. The crystallinities are 43.3, 39.9, 43.6, 42.9, and 36.7% for the PNCs with a particle loading of 0, 3, 5, 8, and 12% respectively. The PNCs exhibit lower $F_c$ as compared to pure PP except for 5 wt % NPs. The lower $F_c$ of the PNCs is attributed to the fact that the NPs are able to disturb the continuity of the polymer matrix and thus introduce more grain boundaries as well as defects, which are also reported previously in high-density polyethylene/MWCNT composites[71,72] and clay reinforced nylon-6 composites.[73]

**3.8. Magnetic Properties.** Figure 14 shows the room temperature magnetic hysteresis loop of the PNCs with a particle loading of 12 wt %. The saturation magnetization ($M_s$) is defined as the state at which an increase in the magnetic field cannot increase the magnetization of the material further. $M_s$ of the PNCs with a particle loading of 12 wt % is estimated to be 6.6 emu/g at a relatively high magnetic field (90 000 Oe). A negligible remanence ($M_r$, the residue magnetization after the applied field is reduced to zero) of 0.14 emu/g and coercivity ($H_c$, the external applied magnetic field necessary to return the material to a zero magnetization condition) of 22.34 Oe are observed, indicating a room temperature soft ferromagnetic behavior of the PNCs.

## 4. CONCLUSION

In this work, a surfactant-free in situ method is introduced to synthesize multifunctional PNCs with high quality dispersion of NPs. The particle size grows up with the increase of particle loading. Results show that the "rheological percolation" is much lower as compared to the "electrical conductivity percolation" owing to the larger effective radius stemmed from the wrapping polymer chains on the particle surface, which also accounts for the uniform dispersion of the NPs. The sharp change in electrical resistivity and dielectric permittivity of the PNCs shows high consistency with each other and both confirm the structural transition starting from 5 wt % particle loading, which is due to the formation of the interparticle network structure (percolation threshold). As a result of the polymer−particle interaction and the oxygen trap of the presence of the metal iron, a significant enhancement in thermal stability of around 120 °C is observed in the PNCs as compared to the p-PP. The magnetic measurement indicates a soft ferromagnetic behavior of these PNCs.

## AUTHOR INFORMATION

### Corresponding Author

*E-mail: zhanhu.guo@lamar.edu. Telephone: (409) 880-7654. Fax: (409) 880-2197.

## ACKNOWLEDGMENT

This project is supported by the National Science Foundation-Nanoscale Interdisciplinary Research Team and Materials Processing and Manufacturing (CMMI-1030755). D.P.Y. acknowledges support from the NSF under Grant No. DMR 04-49022.

## REFERENCES

(1) Wang, Y.; Wei, W.; Maspoch, D.; Wu, J.; Dravid, V. P.; Mirkin, C. A. *Nano Lett.* **2008**, *8*, 3761–3765.
(2) Terris, B. D.; Thomson, T. *J. Phys. D: Appl. Phys.* **2005**, *38*, R199–R222.
(3) Li, G.; Joshi, V.; White, R. L.; Wang, S. X.; Kemp, J. T.; Webb, C.; Davis, R. W.; Sun, S. *J. Appl. Phys.* **2003**, *93*, 7557–7559.
(4) Guo, Z.; Park, S.; Hahn, H. T.; Wei, S.; Moldovan, M.; Karki, A. B.; Young, D. P. *Appl. Phys. Lett.* **2007**, *90*, 053111.
(5) Guo, Z.; Hahn, H. T.; Lin, H.; Karki, A. B.; Young, D. P. *J. Appl. Phys.* **2008**, *104*, 014314.
(6) Lee, J. H.; Huh, Y. M.; Jun, Y.-W.; Seo, J.-W.; Jang, J.-T.; Song, H.-T.; Kim, S.; Cho, E.-J.; Yoon, H.-G.; Suh, J.-S.; Cheon, J. *Nat. Med.* **2007**, *13*, 95–99.
(7) Lu, Z.; Prouty, M. D.; Guo, Z.; Golub, V. O.; Kumar, C. S. S. R.; Lvov, Y. M. *Langmuir* **2005**, *21*, 2042–2050.
(8) Ban, Z.; A. Barnakov, Y.; Li, F.; O. Golub, V.; J. O'Connor, C. *J. Mater. Chem.* **2005**, *15*, 4660–4662.
(9) Gupta, A. K.; Gupta, M. *Biomaterials* **2004**, *26*, 3995–4021.
(10) Zhang, D.; Wei, S.; Kaila, C.; Su, X.; Wu, J.; Karki, A. B.; Young, D. P.; Guo, Z. *Nanoscale* **2010**, *2*, 917–919.
(11) Kim, P.; Doss, N. M.; Tillotson, J. P.; Hotchkiss, P. J.; Pan, M.-J.; Marder, S. R.; Li, J.; Calame, J. P.; Perry, J. W. *ACS Nano* **2009**, *3*, 2581–2592.
(12) Zhu, J.; Wei, S.; Alexander, M., Jr.; Dang, T. D.; Ho, T. C.; Guo, Z. *Adv. Func. Mater.* **2010**, *18*, 3076–3084.
(13) Zhu, J.; Wei, S.; Ryu, J.; Budhathoki, M.; Liang, G.; Guo, Z. *J. Mater. Chem.* **2010**, *20*, 4937–4948.
(14) Zhu, J.; Wei, S.; Ryu, J.; Sun, L.; Luo, Z.; Guo, Z. *ACS Appl. Mater. Interfaces* **2010**, *2*, 2100–2107.
(15) Guo, Z.; Park, S.; Hahn, H. T.; Wei, S.; Moldovan, M.; Karki, A. B.; Young, D. P. *J. Appl. Phys.* **2007**, *101*, 09M511.
(16) Guo, Z.; Lee, S. E.; Kim, H.; Park, S.; Hahn, H. T.; Karki, A. B.; Young, D. P. *Acta Mater.* **2009**, *57*, 267–277.
(17) Shimada, T.; Ookubo, K.; Komuro, N.; Shimizu, T.; Uehara, N. *Langmuir* **2007**, *23*, 11225–11232.
(18) Tseng, C.-H.; Wang, C.-C.; Chen, C.-Y. *Chem. Mater.* **2006**, *19*, 308–315.
(19) Tasis, D.; Tagmatarchis, N.; Bianco, A.; Prato, M. *Chem. Rev.* **2006**, *106*, 1105–1136.
(20) Yang, Y.; Xie, X.; Yang, Z.; Wang, X.; Cui, W.; Yang, J.; Mai, Y.-W. *Macromolecules* **2007**, *40*, 5858–5867.
(21) Guo, Z.; Pereira, T.; Choi, O.; Wang, Y.; Hahn, H. T. *J. Mater. Chem.* **2006**, *16*, 2800–2808.
(22) Kataby, G.; Prozorov, T.; Koltypin, Y.; Cohen, H.; Sukenik, C. N.; Ulman, A.; Gedanken, A. *Langmuir* **1997**, *13*, 6151–6158.

(23) Boyer, C.; Bulmus, V.; Priyanto, P.; Teoh, W. Y.; Amal, R.; Davis, T. P. *J. Mater. Chem.* **2009**, *19*, 111–123.
(24) Lu, Y.; Yin, Y.; Mayers, B. T.; Xia, Y. *Nano Lett.* **2002**, *2*, 183–186.
(25) Guo, Z.; Park, S.; Wei, S.; Pereira, T.; Moldovan, M.; Karki, A. B.; Young, D. P.; Hahn, H. T. *Nanotechnology* **2007**, *18*, 335704.
(26) Pötschke, P.; Fornes, T. D.; Paul, D. R. *Polymer* **2002**, *43*, 3247–3255.
(27) Zhu, J.; Wei, S.; Yadav, A.; Guo, Z. *Polymer* **2010**, *51*, 2643–2651.
(28) Kotsilkova, R.; Fragiadakis, D.; Pissis, P. *J. Polym. Sci., Part B: Polym. Phys.* **2005**, *43*, 522–533.
(29) Kim, H.; Macosko, C. W. *Polymer* **2009**, *50*, 3797–3809.
(30) Sun, L.; Boo, W.-J.; Liu, J.; Clearfield, A.; Sue, H.-J.; Verghese, N. E.; Pham, H. Q.; Bicerano, J. *Macromol. Mater. Eng.* **2009**, *294*, 103–113.
(31) Hyun, Y. H.; Lim, S. T.; Choi, H. J.; Jhon, M. S. *Macromolecules* **2001**, *34*, 8084–8093.
(32) Pötschke, P.; Abdel-Goad, M.; Alig, I.; Dudkin, S.; Lellinger, D. *Polymer* **2004**, *45*, 8863–8870.
(33) Sandler, J. K. W.; Kirk, J. E.; Kinloch, I. A.; Shaffer, M. S. P.; Windle, A. H. *Polymer* **2003**, *44*, 5893–5899.
(34) Kirkpatrick, S. *Rev. Mod. Phys.* **1973**, *45*, 574.
(35) Zallen, R. *The Physics of Amorphous Solids*; Wiley: New York, 1983.
(36) Smith, T. W.; Wychick, D. *J. Phys. Chem.* **1980**, *84*, 1621–1629.
(37) Van Wonterghem, J.; Mørup, S.; Charles, S. W.; Wells, S.; Villadsen, J. *Phys. Rev. Lett.* **1985**, *55*, 410.
(38) Luo, Z. P. *Acta Mater.* **2006**, *54*, 47–58.
(39) Qin, H.; Zhang, S.; Zhao, C.; Hu, G.; Yang, M. *Polymer* **2005**, *46*, 8386–8395.
(40) Li, L.; Li, G.; Smith, R. L.; Inomata, H. *Chem. Mater.* **2000**, *12*, 3705–3714.
(41) Battisha, I. K.; Afify, H. H.; Ibrahim, M. *J. Magn. Magn. Mater.* **2006**, *306*, 211–217.
(42) Sidorov, S. N.; Bronstein, L. M.; Davankov, V. A.; Tsyurupa, M. P.; Solodovnikov, S. P.; Valetsky, P. M.; Wilder, E. A.; Spontak, R. J. *Chem. Mater.* **1999**, *11*, 3210–3215.
(43) Gu, J.; Li, S.; Wang, E.; Li, Q.; Sun, G.; Xu, R.; Zhang, H. *J. Solid State Chem.* **2009**, *182*, 1265–1272.
(44) Oprea, C.; Viorel, I. *Ovidius Univ. Ann. Chem.* **2009**, *20*, 222–226.
(45) Barrau, S.; Demont, P.; Perez, E.; Peigney, A.; Laurent, C.; Lacabanne, C. *Macromolecules* **2003**, *36*, 9678–9680.
(46) Meincke, O.; Kaempfer, D.; Weickmann, H.; Friedrich, C.; Vathauer, M.; Warth, H. *Polymer* **2004**, *45*, 739–748.
(47) Auriemma, F.; De Rosa, C. *Macromolecules* **2002**, *35*, 9057–9068.
(48) Foresta, T.; Piccarolo, S.; Goldbeck-Wood, G. *Polymer* **2001**, *42*, 1167–1176.
(49) Mezghani, K.; Phillips, P. J. *Polymer* **1995**, *36*, 2407–2411.
(50) Mezghani, K.; Phillips, P. J. *Polymer* **1998**, *39*, 3735–3744.
(51) Huxtable, S. T.; Cahill, D. G.; Shenogin, S.; Xue, L.; Ozisik, R.; Barone, P.; Usrey, M.; Strano, M. S.; Siddons, G.; Shim, M.; Keblinski, P. *Nat. Mater.* **2003**, *2*, 731–734.
(52) Fang, D.; Huang, K.; Liu, S.; Luo, Z.; Qing, X.; Zhang, Q. *J. Alloys Compd.* **2010**, *498*, 37–41.
(53) Zou, X. D.; Sukharev, Y.; Hovmoller, S. *Ultramicroscopy* **1993**, *49*, 147–158.
(54) Mikutta, C.; Mikutta, R.; Bonneville, S.; Wagner, F.; Voegelin, A.; Christl, I.; Kretzschmar, R. *Geochim. Cosmochim. Acta* **2008**, *72*, 1111–1127.
(55) Mitchell, C. A.; Bahr, J. L.; Arepalli, S.; Tour, J. M.; Krishnamoorti, R. *Macromolecules* **2002**, *35*, 8825–8830.
(56) Poslinski, A. J.; Ryan, M. E.; Gupta, R. K.; Seshadri, S. G.; Frechette, F. J. *J. Rheol.* **1988**, *32*, 703–735.
(57) Ugaz, V. M.; Cinader, D. K.; Burghardt, W. R. *Macromolecules* **1997**, *30*, 1527–1530.
(58) Shenoy, A. V. *Rheology of filled polymer systems*. Kluwer Academic Publishers: Dordrecht, The Netherlands, 1999.
(59) Du, F.; Scogna, R. C.; Zhou, W.; Brand, S.; Fischer, J. E.; Winey, K. I. *Macromolecules* **2004**, *37*, 9048–9055.
(60) Krishnamoorti, R.; Giannelis, E. P. *Macromolecules* **1997**, *30*, 4097–4102.
(61) McNally, T.; Pötschke, P.; Halley, P.; Murphy, M.; Martin, D.; Bell, S. E. J.; Brennan, G. P.; Bein, D.; Lemoine, P.; Quinn, J. P. *Polymer* **2005**, *46*, 8222–8232.
(62) Wu, X.; Xu, Q.; Shang, S.; Shui, J.; Liu, C.; Zhu, Z. *Chin. Phys. Lett.* **2008**, *25*, 1388–1391.
(63) Bower, D. I. *An Introduction to Polymer Physics*. Cambridge University Press: New York, 2002.
(64) Chen, X.; Wei, S.; Yadav, A.; Patil, R.; Zhu, J.; Ximenes, R.; Sun, L.; Guo, Z. *Macromol. Mater. Eng.* **2011**10.1002/mame.201000341.
(65) Dang, Z. M.; Wang, L.; Yin, Y.; Zhang, Q.; Lei, Q. Q. *Adv. Mater.* **2007**, *19*, 852–857.
(66) Ge, J. J.; Hou, H.; Li, Q.; Graham, M. J.; Greiner, A.; Reneker, D. H.; Harris, F. W.; Cheng, S. Z. D. *J. Am. Chem. Soc.* **2004**, *126*, 15754–15761.
(67) Kashiwagi, T.; Du, F.; Douglas, J. F.; Winey, K. I.; Harris, R. H.; Shields, J. R. *Nat. Mater.* **2005**, *4*, 928–933.
(68) Agag, T.; Koga, T.; Takeichi, T. *Polymer* **2001**, *42*, 3399–3408.
(69) Zhu, J.; Morgan, A. B.; Lamelas, F. J.; Wilkie, C. A. *Chem. Mater.* **2001**, *13*, 3774–3780.
(70) Yuan, Q.; Misra, R. D. K. *Polymer* **2006**, *47*, 4421–4433.
(71) Yang, J.; Wang, C.; Wang, K.; Zhang, Q.; Chen, F.; Du, R.; Fu, Q. *Macromolecules* **2009**, *42*, 7016–7023.
(72) Kodjie, S. L.; Li, L.; Li, B.; Cai, W.; Li, C. Y.; Keating, M. *J. Macromol. Sci. Part B Phys.* **2006**, *45*, 231–245.
(73) Fornes, T. D.; Paul, D. R. *Polymer* **2003**, *44*, 3945–3961.